Nano Research

Open Access

Research Article

Ultrafast-explosion-driven carbon nanoreactors embedding high-entropy alloy electrocatalysts for efficient oxygen evolution reaction

Xindong Zhu[1,§], Fan Xue[1,§], He Zhu[1,2] ✉, Wen Huang[1], Haoran Yu[1], Simiao Peng[1], Wei-Di Liu[1], Ruohan Yu[3] ✉, Jianrong Zeng[4,5], and Si Lan[1,2] ✉

[1] *Herbert Gleiter Institute of Nanoscience, School of Materials Science and Engineering, Nanjing University of Science and Technology, Nanjing 210094, China*
[2] *Key Laboratory of Advanced Nano Structures and Functional Materials Jiangsu Province Universities, Nanjing 210094, China*
[3] *The Sanya Science and Education Innovation Park, Wuhan University of Technology, Sanya 572000, China*
[4] *Shanghai Synchrotron Radiation Facility, Shanghai Advanced Research Institute, Chinese Academy of Sciences, Shanghai 201204, China*
[5] *Shanghai Institute of Applied Physics, Chinese Academy of Sciences, Shanghai 201800, China*
§ *Xindong Zhu and Fan Xue contributed equally to this work.*

Cite this article: *Nano Research*, **2026**, *19*, 94908613. https://doi.org/10.26599/NR.2026.94908613

ABSTRACT: High-entropy alloy (HEA) electrocatalysts offer tunable multi-element synergy and intrinsic structural robustness for oxygen evolution reaction (OER), yet integrating high active-site exposure with desirable lattice and electronic structures remains a significant challenge. Here we present an ultrafast thermal explosion strategy for one-step synthesis of carbon-encapsulated nanoreactors uniformly embedding FeCoNiCuAl HEA nanoparticles. Ultrafast heating of metal-chloride-loaded carbon black drives rapid chloride decomposition and gas evolution, inflating the carbon into a hierarchical porous network and inducing the formation and spatial confinement of HEA nanoparticles. This nanoreactor architecture with confined microenvironments maximizes accessible active sites and accelerates mass/charge transport, yielding lower OER overpotentials than commercial RuO_2. Its applicabilities in overall water splitting (OWS) and rechargeable Zn-air batteries further confirm the potential for practical energy storage integration. Local structural investigations reveal that the incorporation of Al element could reduce the first-shell coordination number, enhancing the adsorption capacity of the active sites. Density functional theory (DFT) calculations further demonstrate that the synergistic interaction between Al and neighboring metal sites facilitates the efficient OER, and Al-induced modulation of electronic structure lowers the desorption barrier of the *OOH intermediate, thereby accelerating OER kinetics. This explosion-driven nanoreactor strategy provides a general and one-step route to engineer carbon nanoreactors embedding HEA electrocatalysts, opening new avenues for advanced clean energy catalysis and practical device integration.

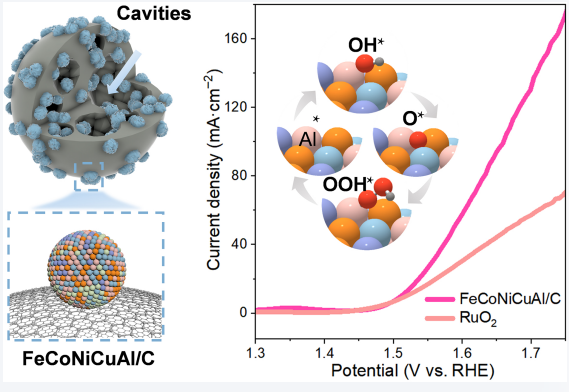

KEYWORDS: electrochemistry, high-entropy alloys, oxygen evolution reaction, Joule heating synthesis, synchrotron X-ray techniques

1 Introduction

Electrocatalytic water splitting is an essential route for sustainable hydrogen production, whose efficiency remains constrained by the sluggish kinetics of the oxygen evolution reaction (OER) at anode [1–4]. The inherent complex four-electron transfer pathway, involving multiple intermediate species (e.g., *OH, *O, and *OOH) [5], requires electrocatalysts capable of optimizing adsorption energies across reaction steps while maintaining structural robustness under oxidative conditions [6]. Currently, commercial OER electrocatalysts are predominantly noble-metal-based electrocatalysts, such as IrO_2 and RuO_2 [7, 8]. Despite their high activity, the scarcity and high cost severely hinder their large-scale applications [9]. Large-scale applications are not only relevant to electrocatalytic water splitting but also to rechargeable Zn-air

Received: November 16, 2025; **Revised:** February 28, 2026
Accepted: March 2, 2026

✉Address correspondence to He Zhu, hezhu@njust.edu.cn; Ruohan Yu, yuruohan@whut.edu.cn; Si Lan, lansi@njust.edu.cn

batteries (ZABs), since the OER plays a crucial role in rechargeable Zn-air batteries by governing the charging process efficiency [10]. Therefore, the development of noble-metal-free OER electrocatalysts with high activity, stability, and cost-effectiveness is of great significance to extend the application of water splitting and Zn-air batteries [11].

High-entropy alloys (HEAs), comprising five or more elements in a single-phase solid solution, have recently gained attention as promising noble-metal-free OER electrocatalysts [12–15]. Their unique "cocktail effect" enables synergistic interactions among constituent elements, offering tunable d-band electronic structures and distortion-induced strain fields [16, 17]. This is critical for regulating and stabilizing reactive intermediates [18–20]. Despite their inherent advantages, conventional HEA synthesis strategies face persistent limitations in synergistically optimizing electronic structures and ensuring high-density active site exposure. To address these challenges, various synthetic methods have been developed to disperse HEA nanoparticles (NPs) onto low-dimensional carbon supports (e.g., carbon nanotubes and graphene) [21, 22], including conventional high-temperature alloying [23], liquid-phase synthesis [24], and gas-phase synthesis strategy [25]. For instance, Luo et al. employed ligand-assisted interfacial assembly combined with NH_3 annealing to fabricate ordered HEA NPs on a two-dimensional (2D) nitrogen-rich mesoporous carbon framework, achieving high electrocatalytic activity and durability [26]. Nevertheless, these approaches often lack precise control over nanoparticle dispersion and catalyst–support interfaces, thereby constraining active-site exposure and electron/mass transport. Therefore, a facile and innovative approach is urgently needed to maximize active-site density while optimize electronic structure of HEA electrocatalysts.

In this work, we propose a one-step ultrafast thermal explosion synthesis via carbon thermal shock (CTS) to engineer hierarchically porous nanoreactors uniformly embedding FeCoNiCuAl HEA NPs. A heating rate of ~ 10^3 K·s^{-1} triggers rapid metal-chloride decomposition and gas evolution, which simultaneously inflates the carbon matrix into an interconnected cavity network and nucleate well-dispersed HEA NPs. Moreover, the extreme non-equilibrium environment of CTS provides a powerful platform to tailor atomic coordination and electronic structures into high-energy states [27–31]. Comprehensive structural and spectroscopic analyses confirm robust nanoparticle confinement and Al-driven modulation of surface coordination and electronic states. Complementary density functional theory (DFT) calculations reveal that the adsorption sites dynamically shift during the OER process, and Al and neighboring metal sites synergistically collaborate to complete the OER process. Al incorporation leads to a significantly reduced free-energy barrier for *OOH desorption, indicating the enhanced OER kinetics. Beyond realizing exceptional OER activity and stability, this ultrafast thermal explosion strategy establishes a versatile route for accessing metastable alloys and designing hierarchical porous architectures, paving the way for broad applications in electrocatalysis, energy storage, and advanced materials engineering.

2 Experimental section

2.1 Synthesis of the FeCoNiCuAl/C nanoreactors

In an argon-filled glove box, an equimolar mixture of the metal chloride precursors ($FeCl_3·6H_2O$, 0.27 g; $CoCl_2·6H_2O$, 0.24 g; $NiCl_2·6H_2O$, 0.24 g; $CuCl_2·2H_2O$, 0.17 g; and $AlCl_3·6H_2O$, 0.24 g) was thoroughly mixed with carbon black (0.3 g) and ground for 30 min. Next, the homogeneous powders were then pressed into a thin film on carbon paper and clamped onto a copper stage inside the CTS equipment (HTS-7026D, Shenzhen Zhongke Jingyan Technology Co., Ltd.) under an Ar atmosphere. A pulsed current of 90 A at 32 V was applied, heating the sample to ~ 1273 K within milliseconds. During this high-temperature treatment, the release of gaseous byproducts (e.g., Cl_2) from salt decomposition, along with minor handling losses during sample transfer, resulted in a final yield of approximately 0.3 g of the FeCoNiCuAl/C nanoreactors. The resulting products were collected and stored under inert atmosphere until characterization.

2.2 Characterizations

X-ray diffraction (XRD) patterns were recorded on a Bruker-AXS D8 Advance diffractometer (Cu Kα, λ = 1.5406 Å) over 2θ = 20°–100° at 0.05° per second. Field-emission scanning electron microscopy (SEM, JSM-7800F PRIME, 5 kV) and transmission electron microscopy (TEM, JEOL JEM-2100F, 200 kV) were used to examine theparticle size, dispersion, and carbon architecture. The decomposition temperature of 810 K was probed by thermogravimetric analysis equipped with differential scanning calorimetry (TGA-DSC, TGA/DSC3+) from room temperature to 1273 K at 50 K·min^{-1} under Ar. Elemental composition was determined using inductively coupled plasma mass spectrometry (ICP-MS). The Brunauer–Emmett–Teller (BET) method was utilized to determine the specific surface area. The Raman spectra were recorded using a LabRAM HR Evolution Raman spectrometer with a 532 nm laser wavelength.

High-angle annular dark-field scanning TEM (HAADF-STEM), energy dispersive X-ray (EDX) mapping, and three-dimensional (3D) tomographic reconstruction experiments were conducted using a probe-corrected FEI Themis TEM instrument (operated at 300 kV). A Gatan image filter spectrometer was utilized for data collection. A probe convergence angle of 17.8 mrad and a probe current of ~ 10 pA were employed for STEM-EDX data collection. Tilt series (−80° to +80°) were acquired using a Fischione tomography holder. The resulting tomographic data was reconstructed using Thermo Fisher 3D Inspect software and then visualized using Avizo.

2.3 Synchrotron X-ray scattering and absorption spectroscopy techniques

Synchrotron X-ray total scattering measurements were performed at the BL13SSW beamline of the Shanghai Synchrotron Radiation Facility (SSRF). The center energy of the beamline X-rays was 50.00 keV, corresponding to a wavelength λ = 0.2480 Å. The two-dimensional scattering images were calibrated and integrated using Dioptas software [32]. The pair distribution function (PDF) patterns were converted from the resulting one-dimensional data using PDFgetX2 software for background deduction and corrections, and the $G(r)$ functions were computed by Fourier transform (Q_{max} = 16.8 Å^{-1}) [33]. The unit cell parameters of the FeCoNiCuAl/C and FeCoNiCu/C were refined by small box fitting based on PDFgui [34].

In order to obtain the average local coordination structure of the FeCoNiCuAl/C and FeCoNiCu/C, the X-ray absorption fine structure (XAFS) spectra of the Fe K-edge, Co K-edge, Ni K-edge,

and Cu K-edge were also collected at the BL13SSW of the SSRF. The data about the Fe K-edge (E = 7112 eV), Co K-edge (E = 7709 eV), Ni K-edge (E = 8333 eV), and Cu K-edge (E = 8979 eV) were collected at room temperature in transmission mode. The Athena software package processed the raw data, and the extended X-ray absorption fine structure (EXAFS) oscillation function was fitted by Artemis software [35]. Wavelet transform (WT) of the Fe K-edge, Co K-edge, Ni K-edge, and Cu K-edge EXAFS oscillations were implemented using HAMA software module developed by Harald and Marina Chukalina [36].

2.4 Electrochemical tests

Electrochemical measurements were conducted in a three-electrode electrochemical cell using a Pt sheet as the counter electrode and Ag/AgCl as the reference electrodes, with a salt bridge employed to minimize potential interactions between hydroxide ions (OH^-) and the AgCl surface [37]. A 1 M KOH solution was used as the electrolyte, with the actual pH values measured experimentally at 13.6. The reference electrode potential was converted to the reversible hydrogen electrode (RHE) scale using Eq. (1)

$$E(\mathrm{RHE}) = E(\mathrm{Ag/AgCl}) + 0.197\ \mathrm{V} + 0.0592 \times \mathrm{pH} \quad (1)$$

Linear sweep voltammetry (LSV) was tested from 1.2 to 1.8 V (vs. RHE) at a scan rate of 10 mV·s^{-1}, with 100% *iR* compensation after activating the working electrode for several times until stable signals were achieved. The electrochemical double-layer capacitance (C_{dl}) was determined by cyclic voltammetry (CV) in the non-Faradaic region (0.02–0.12 V vs. Ag/AgCl) at scan rates of 20, 40, 60, 80, 100, and 120 mV·s^{-1}. This method was utilized to estimate the electrochemically active surface area (ECSA). Electrochemical impedance spectroscopy (EIS) measurements were recorded at 1.5 V (vs. RHE) over a frequency range from 100 kHz to 0.1 Hz with an alternating current (AC) amplitude of 5 mV. Oxygen reduction reaction (ORR) polarization curve was tested from 0.4 to 1.0 V (vs. RHE) at a scan rate of 10 mV·s^{-1}.

The overall water splitting was constructed using commercial 20 wt.% Pt/C loaded on carbon cloth (1.0 mg·cm^{-2}) as the cathode and carbon cloth coated with 1.0 mg·cm^{-2} of the catalyst as the anode, immersed in a flowing alkaline electrolyte (1.0 M KOH). Polarization curves were measured at a scan rate of 10 mV·s^{-1} and the chronopotentiometry measurements were collected at a current density of 10 mA·cm^{-2}.

A rechargeable Zn-air battery was assembled with a polished zinc foil as the anode and carbon paper coated with 1.0 mg·cm^{-2} of the catalyst as the air cathode, with a aqueous electrolyte consisting of 6.0 M KOH and 0.2 M $ZnCl_2$. The Pt/C + RuO_2 (mass ratio of 1:1) mixture was used as the benchmark catalyst. Polarization curves were measured at a scan rate of 5 mV·s^{-1} and the galvanostatic charge/discharge cycling measurements were collected at a current density of 10 mA·cm^{-2}.

2.5 Computational method

The first principles calculations employed DFT using projector augmented wave (PAW) method with the Vienna *ab initio* simulation package (VASP) code. Exchange-correlation effects are treated within the Perdew–Burke–Ernzerhof (PBE) of the generalized gradient approximation (GGA) and the spin-orbit interaction included. The energy is converged to 10^{-5} eV with a plane-wave energy cutoff of 450 eV and 6 × 3 × 1 k points generated in a Gamma centred grid [38]. The HEA structure containing 135 atom supercell was populated with metal atoms (Fe, Co, Ni, Cu, and Al) based on experimental compositions. The alloy theoretic automated toolkit (ATAT) software package was used to distribute transition metals across sites in a special quasirandom structure (SQS) [39]. The surface of HEA with low energy (111) orientation was modeled in which a 9-layered HEA (111) slab. At least 15 Å vacuum in stacking direction was added to separate the free surfaces of HEA due to periodic.

3 Results and discussion

FeCoNiCuAl/C nanoreactors were synthesized by CTS of carbon paper loaded with a mixture of carbon black (CB) and equimolar Fe, Co, Ni, Cu, and Al chloride precursors under an Ar atmosphere (Fig. S1 in the Electronic Supplementary Material (ESM), see details in Section 2). Upon applying 90 A at 32 V, the sample was heated to ~ 1273 K within milliseconds, corresponding to a heating rate of ~ 10^3 K·s^{-1} (Fig. S2 in the ESM). TGA-DSC analysis shows that most metal chlorides decompose between 810 and 1030 K, liberating gaseous byproducts (e.g., Cl_2) that trigger an explosion-like expansion of the carbon matrix and create interconnected hollow cavities (Fig. S3 in the ESM). During the rapid cooling stage (~ 10^3 K·s^{-1}), the vaporized metal species condense and intermix under non-equilibrium conditions, leading to *in situ* nucleation and uniform confinement of FeCoNiCuAl HEA NPs within the porous carbon framework. This one-step CTS process thus yields hierarchically porous nanoreactors featuring continuous internal porosity and well-dispersed HEA electrocatalysts. A schematic diagram illustrating our proposed ultrafast thermal explosion strategy is presented in Fig. 1(a). For comparison, FeCoNiCu/C and Co/C samples were also prepared using similar operational procedures.

The crystal structure of the FeCoNiCuAl HEA electrocatalyst was first determined by XRD. As shown in Fig. S4(a) in the ESM, FeCoNiCuAl, FeCoNiCu, and Co all adopt a face-centered cubic (FCC) lattice. Notably, the diffraction peak for FeCoNiCuAl shifts to a higher 2θ angle compared to FeCoNiCu (Fig. S4(b) in the ESM), indicating a lattice contraction with the addition of Al. Rietveld refinement of the XRD data yields a lattice parameter of a = 3.557 Å for FeCoNiCuAl (Fig. 1(b)). The reduction in lattice parameter from FeCoNiCu (3.561 Å) to FeCoNiCuAl confirms a lattice contraction upon Al incorporation, consistent with the observed 2θ angle shift toward higher angles (Fig. S5 in the ESM). To probe local structure, we carried out full-profile PDF refinement using synchrotron X-ray total scattering data (Fig. 1(c)). The resulted first-shell metal–metal distance (2.537 Å) deviates slightly from the ideal FCC bond length, implying the presence of local distortions. Such deviations are consistent with surface reconstruction on the HEA NPs, where atomic-scale strain fields and element size mismatch induce non-uniform lattice environments, contributing to enhanced electrochemical activity [40].

The SEM image of the FeCoNiCuAl/C reveals that the CB particles maintains their well-preserved spherical morphology with an average diameter of ~ 50 nm (Fig. S6 in the ESM). FeCoNiCuAl NPs with an average size of ~ 7.40 nm are embedded within the carbon matrix (Fig. 1(d) and Fig. S7 in the ESM). Notably, as shown in Fig. S8 in the ESM, the particle size of the FeCoNiCu NPs is approximately 18 nm, which is larger than that of the FeCoNiCuAl NPs. This suggests that the addition of Al modifies

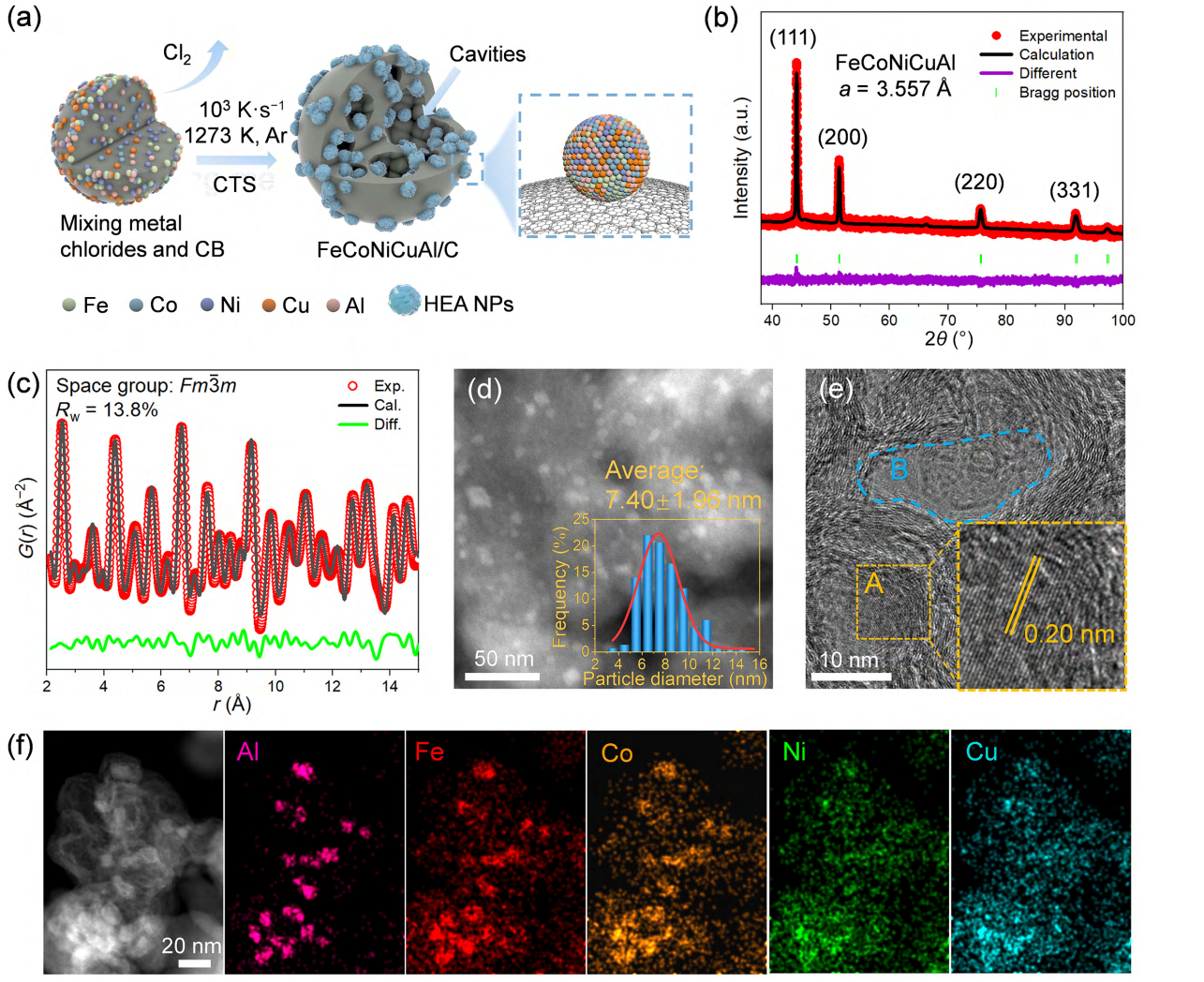

Figure 1 (a) Schematic illustration of the one-step CTS process for synthesizing hierarchically porous FeCoNiCuAl HEA nanoreactors. (b) Rietveld refinement of the XRD pattern for the FeCoNiCuAl HEA electrocatalyst, fitted to a cubic FCC $Fm\bar{3}m$ model. (c) Full-profile PDF refinement of FeCoNiCuAl HEA electrocatalyst using cubic $Fm\bar{3}m$ model. (d) Dark-field TEM image of FeCoNiCuAl HEA NPs uniformly dispersed on the carbon support. The inset shows particle-size histogram obtained by counting 50 NPs. (e) HRTEM image of FeCoNiCuAl loaded nanoreactor. The inset displays lattice fringes corresponding to the (111) planes of the FCC HEA phase. (f) HAADF-STEM image and the corresponding EDS mapping of Fe, Co, Ni, Cu, and Al in FeCoNiCuAl NPs.

the particle morphology. From the high-resolution TEM (HRTEM) image (Fig. 1(e)), distinct lattice fringes with a spacing of 0.20 nm (region A) could be observed, corresponding to the (111) plane of the FCC FeCoNiCuAl HEA. Additionally, region B in the HRTEM image shows the presence of cavities with the carbon matrix, which is expected to promote electrolyte accessibility and enhance active-site utilization within the HEA electrocatalyst. HAADF image coupled with energy dispersive X-ray spectroscopy (EDS) elemental mapping (Fig. 1(f) and Fig. S9 in the ESM) demonstrate that Fe, Co, Ni, Cu, and Al are uniformly distributed within HEA NPs, without apparent phase separation observed. Simultaneously, a portion of the Fe, Co, Ni, and Cu signals is also discernible on the carbon support, indicating that during the ultrafast thermal explosion synthesis process, a minor fraction of metal species is dispersed in the form of nanoscale clusters within the carbon matrix (Fig. S10 in the ESM). This observation is consistent with the inherent characteristics of this synthesis method [41, 42]. This distribution, combined with the mesoporous structure, is expected to be beneficial to enhancing electrocatalytic performance of the FeCoNiCuAl/C electrocatalyst.

Moreover, the EDS analysis further confirmed that the atomic ratio of Fe, Co, Ni, Cu, and Al is approximately 18:20:23:17:22, which is consistent with the results obtained from inductively coupled plasma (ICP) analysis (Table S1 in the ESM). Based on the ICP-MS-measured compositions, we calculated the configurational mixing entropy (ΔS_{mix}) using the equation of $\Delta S_{mix} = -R\Sigma(x_i \ln x_i)$, where R is the molar gas constant, and x_i represents the atomic fraction of each element. The calculated ΔS_{mix} value (~ 1.59R) surpasses the threshold of 1.5R commonly recognized for HEAs, confirming that FeCoNiCuAl/C catalyst meets the criteria for HEA classification. This hierarchical architecture (HEA NPs and cavities within the carbon matrix) functions as an efficient nanoreactor, where confinement effects facilitate sufficient contact between the electrolyte and active sites.

The OER performance of FeCoNiCuAl/C and reference samples was evaluated in O_2-saturated 1 M KOH using a typical three-electrodes cell. As shown in Fig. 2(a), FeCoNiCuAl/C achieves the lowest overpotential of 280 mV at 10 mA·cm^{-2}, superior than commercial RuO_2 (295 mV), FeCoNiCu/C (300 mV), and Co/C (346 mV). The activity enhancement of FeCoNiCuAl/C persists at

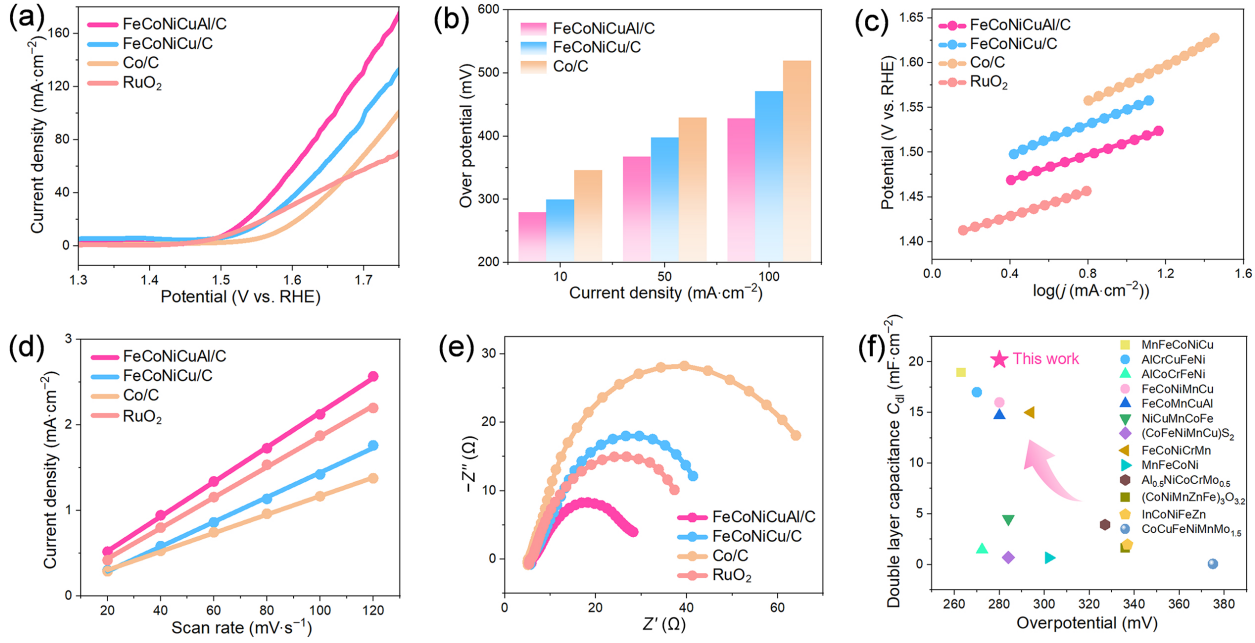

Figure 2 Electrocatalytic OER performances of FeCoNiCuAl/C electrocatalyst. (a) LSV polarization curves in O_2-saturated 1 M KOH. (b) Overpotentials at 10, 50, and 100 mA·cm^{-2} for FeCoNiCuAl/C, FeCoNiCu/C, Co/C, and commercial RuO_2. (c) Tafel plots derived from LSV data. (d) C_{dl} capacitances and (e) EIS Nyquist plots of FeCoNiCuAl/C, FeCoNiCu/C, Co/C, and commercial RuO_2. (f) Comparison of both overpotential at 10 mA·cm^{-2} and double-layer capacitance of previously reported noble-free HEA electrocatalysts.

higher current densities (50 and 100 mA·cm^{-2}), indicating the robustness of the electrocatalyst (Fig. 2(b)). In contrast, the non-porous CB substrate exhibits negligible activity (Fig. S11 in the ESM). Kinetic analysis (Fig. 2(c)) yields a Tafel slope of 70.9 mV·dec^{-1} for FeCoNiCuAl/C, considerably lower than FeCoNiCu/C (83.92 mV·dec^{-1}), Co/C (106.82 mV·dec^{-1}), and commercial RuO_2 (86.31 mV·dec^{-1}), indicating more favorable OER kinetics. The C_{dl} extracted from non-Faradaic CV (Fig. 2(d) and Fig. S12 in the ESM) is 20.2 mF·cm^{-2} for FeCoNiCuAl/C, higher than that for FeCoNiCu/C (14.4 mF·cm^{-2}), Co/C (10.8 mF·cm^{-2}), and RuO_2 (17.8 mF·cm^{-2}), corresponding to ECSA values of 505, 360, 270, and 445 cm^2, respectively (Fig. S13 in the ESM). These results confirm that the hierarchically porous nanoreactor design maximizes accessible active sites. Notably, Al itself is intrinsically inactive in OER, yet its incorporation into the FeCoNiCu/C matrix markedly enhances performance. This boost may arise from Al-induced electronic modulation that optimizes the adsorption energy of key intermediates, a mechanism we further elucidate through XAFS and DFT studies below.

EIS was employed to probe charge-transfer behavior under OER conditions. Nyquist plots for all samples feature a large semicircle in the low-frequency region (Fig. 2(e)), whose diameter corresponds to the charge transfer resistance (R_{ct}). The FeCoNiCuAl/C exhibits the smallest R_{ct}, consistence with its low OER overpotential and accelerated kinetics. Long-term stability was evaluated by chronopotentiometry test at 10 mA·cm^{-2} (Fig. S14 in the ESM). FeCoNiCuAl/C maintains a nearly constant potential over 20 h of continuous operation, demonstrating exceptional durability in alkaline media. To further substantiate the stability of the catalyst, we conducted an ICP measurement to determine the elemental compositions of the FeCoNiCuAl/C following the OER test. The results (Table S1 in the ESM) show that while Al and Cu display a marginal decline in the contents relative to the other elements, the amounts of Fe, Co, and Ni remain relatively constant with only insignificant variations. This phenomenon can be attributed to the severe lattice distortion effect inherent to HEAs, which effectively prevents excessive dissolution of the elements [43]. Considering both overpotential and C_{dl}, our designed explosion-driven FeCoNiCuAl/C nanoreactor has achieved a superior performance level among the noble-metal-free HEA electrocatalysts ever reported (Fig. 2(f)) [11, 12, 18, 27, 44–52].

In view of the good OER activity and stability of FeCoNiCuAl/C, a two-electrode configuration for overall water splitting was assembled using FeCoNiCuAl/C as the anode catalyst and Pt/C as the cathode catalyst. As shown in Fig. S15(a) in the ESM, the FeCoNiCuAl/C||Pt/C achieves a current density of 10 mA·cm^{-2} at 1.56 V, which is much lower than that of RuO_2||Pt/C (1.58 V). The two-electrode system assembled by FeCoNiCuAl/C||Pt/C (1.56 V) was continuously operated for 20 h at a current density of 10 mA·cm^{-2} with a negligible current attenuation (Fig. S15(b) in the ESM). Such a combination of good activity and stability endows it with great potential for practical applications in sustainable hydrogen production.

Furthermore, FeCoNiCuAl/C was evaluated as the air cathode for rechargeable ZABs. Compared to Pt/C + RuO_2 battery, the HEA-based battery exhibits a narrower charge–discharge polarization gap (Fig. S16(a) in the ESM), higher discharge voltage, and lower recharge voltage. Furthermore, its peak power density reaches 108.4 mW·cm^{-2} at 204 mA·cm^{-2}, superior than the 98.9 mW·cm^{-2} achieved by the Pt/C + RuO_2 cell (Fig. S16(b) in the ESM). In addition, as illustrated in Fig. S16(c) in the ESM, the open-circuit potential of the FeCoNiCuAl/C-based battery is estimated to be 1.42 V, slightly higher than that based on Pt/C + RuO_2 (1.41 V). The good ZAB performance is primarily attributed to the superior OER capability, outweighing the impact of the moderate ORR performance, as evidenced by a half-wave potential of 0.72 V (Fig. S17 in the ESM). The HEA/C cathode reliably powers a 2.0 V light-emitting diode (LED), validating its practical applicability (Fig.

S16(d) in the ESM). The operational stability of the FeCoNiCuAl/C cell maintains a steady charge potential (1.95 V), discharging potential (1.19 V), and a round-trip efficiency of 61% for over 80 h without significant deterioration, which is comparable to the Pt/C + RuO_2 system (Fig. S16(e) in the ESM). These results highlight the potential of our designed explosion-driven HEA nanoreactors for high-performance and durable energy storage devices.

Catalytic performance depends critically on two factors: the density of accessible active sites governed by the microstructural architecture, and the intrinsic activity of those sites defined by their local coordination environment [53, 54]. To directly visualize how our explosion-driven CTS process optimizes both aspects, we performed 3D HAADF-STEM tomography reconstruction on FeCoNiCuAl/C. Figure 3(a) presents the front view of the reconstructed volume (240 nm × 254 nm × 312 nm), where the high-contrast regions (yellow) correspond to HEA NPs and low-contrast regions (green) to the CB matrix. The orthogonal slices visualize a continuous and interconnected network of hollow cavities pervading the CB matrix, and the HEA NPs are revealed to be uniformly and intimately bounded to the cavity walls (Fig. 3(b)). By adjusting the contrast range, the low-contrast CB can be filtered and removed for a better visualization of the HEA NPs and cavities (Fig. 3(c) and Fig. S18 in the ESM). The results show that the HEA NPs are uniformly dispersed with a particle size of ~ 4.98 nm, and hollow cavities occupy 28% of the total material volume. Such a hierarchical porosity not only exposes a large number of active sites, consistent with the measured high ECSA of 505 cm^2, but also creates locally concentrated reactant reservoirs, shortening diffusion paths and reducing mass-transfer resistance [55–57]. The tight coupling between nanopores and catalyst particles further ensures efficient electron transfer, as evidenced by the minimal charge-transfer resistance in EIS. Furthermore, Fig. S19 in the ESM shows that the BET surface area of the FeCoNiCuAl/C nanoreactors was measured to be 198.97 m^2, a value that significantly exceeds those of conventional catalysts [58]. This high surface area not only provides abundant active sites but also enhances mass transfer efficiency [59]. Consequently, these microstructural features, i.e., numerous cavities, homogeneous HEA NPs dispersion, and strong HEA–cavity interfaces, provide a superior microstructural platform that ensures the outstanding OER activity and kinetics. Specifically, the nanoscale cavities within the nanoreactor function as concentrated electrolyte reservoirs, creating localized microenvironments of significantly increased OH^- concentrations at catalyst surfaces that accelerate adsorption of OH^- intermediates on active

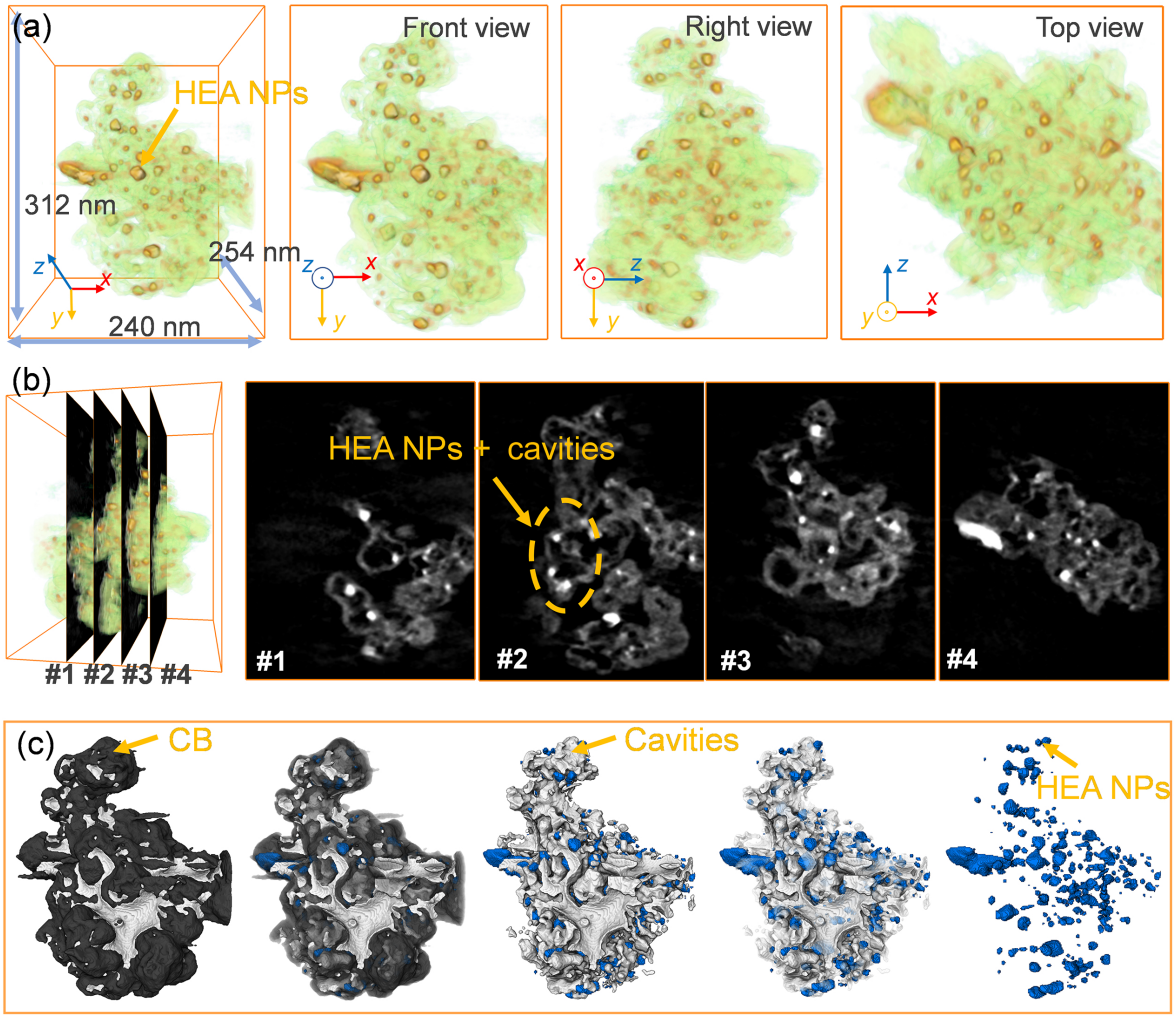

Figure 3 3D tomography reconstruction of FeCoNiCuAl/C nanoreactors. (a) Reconstructed FeCoNiCuAl/C and corresponding front, right, and top views of the same reconstruction. (b) Orthoslices through the volume (*xy* planes at *z* = 69, 99, 129, and 159 nm). (c) Sequential filtering of the reconstructed data for the removal of low-contrast carbon, isolation of cavity structures, and final rendering of HEA nanoparticles

sites of the HEA NPs and effectively lower the activation energy barrier for the OER reaction. Simultaneously, the interconnected hollow structure shortens the diffusion pathway for O_2 gas products, reducing mass transfer resistance and minimizing the accumulation of O_2 bubbles on catalyst surfaces, significantly improving OER performance [60–62].

Atomic pair distribution function (PDF) analysis was conducted to probe the local atomic structure in FeCoNiCuAl/C versus FeCoNiCu/C (Fig. 4(a)). In FeCoNiCuAl/C sample, the first three coordination shells are shifted to shorter interatomic distances compared to the FeCoNiCu/C, which may be related to compressive strains induced by Al incorporation. The corresponding atomic distances could be extracted from full-profile PDF fitting (Fig. S20 in the ESM) and the values are listed in Table S2 in the ESM. However, because Fe, Co, Ni, and Cu scatter X-rays similarly, PDF alone cannot resolve element-specific distortion. With this regard, synchrotron XAFS was employed to investigate electronic and local coordination structures of specific elements. From the XANES data (Figs. 4(b) and 4(c), and Fig. S21 in the ESMN), the metallic states of Fe, Co, Ni, and Cu elements are similar with their corresponding metal foils. In addition, compared to FeCoNiCu/C, the absorption edges of Fe and Cu in the FeCoNiCuAl/C are nearly unchanged. In contrast, the Ni and Co edges shift to lower energies, indicating lower valance states for an electron-rich local environment around those atoms. This electronic enrichment might be attributed to surface-passivating effect of Al that prevent the oxidation of other elements, which could tune the d-band center and facilitate OER kinetics [63, 64].

To probe local bonding environments, we performed wavelet-transform EXAFS (WT-EXAFS) analysis and quantitative EXAFS fitting. The WT-EXAFS maps for Fe, Co, and Ni in FeCoNiCuAl/C exhibit a single intensity maximum at ~ 8.3 $Å^{-1}$, while the WT-EXAFS plot for Cu displays an additional intensity component at higher k of 8.6 $Å^{-1}$ (Fig. 4(d)). These results indicate that Al preferentially bonds with lighter elements (Fe/Co/Ni) rather than heavier element Cu leading to the aggregation of Cu. This behavior aligns with the more negative mixing enthalpies of Fe–Al (−11 $kJ·mol^{-1}$), Co–Al (−19 $kJ·mol^{-1}$) and Ni–Al (−22 $kJ·mol^{-1}$) pairs than the Cu–Al (−1 $kJ·mol^{-1}$) pair [65]. Quantitative EXAFS fittings (Figs. 4(e) and 4(f), and Figs. S22 and S23 in the ESM) and the extracted bond lengths and coordination numbers (Figs. 4(g) and 4(h), and Table S3 in the ESM) reveal contractions of Fe–M, Co–M, and Ni–M but an expansion of Cu–M in FeCoNiCuAl/C relative to those in FeCoNiCu/C, indicating a lattice distortion induced by Al. In addition, the first-shell coordination numbers for all metals are revealed to reduce with the introduction of Al. The resulting low-coordination active sites, together with the Al-induced strain engineering, may optimize the electronic structure, strengthening the adsorption of critical intermediates [66–68], which explains the enhanced OER performance of FeCoNiCuAl/C.

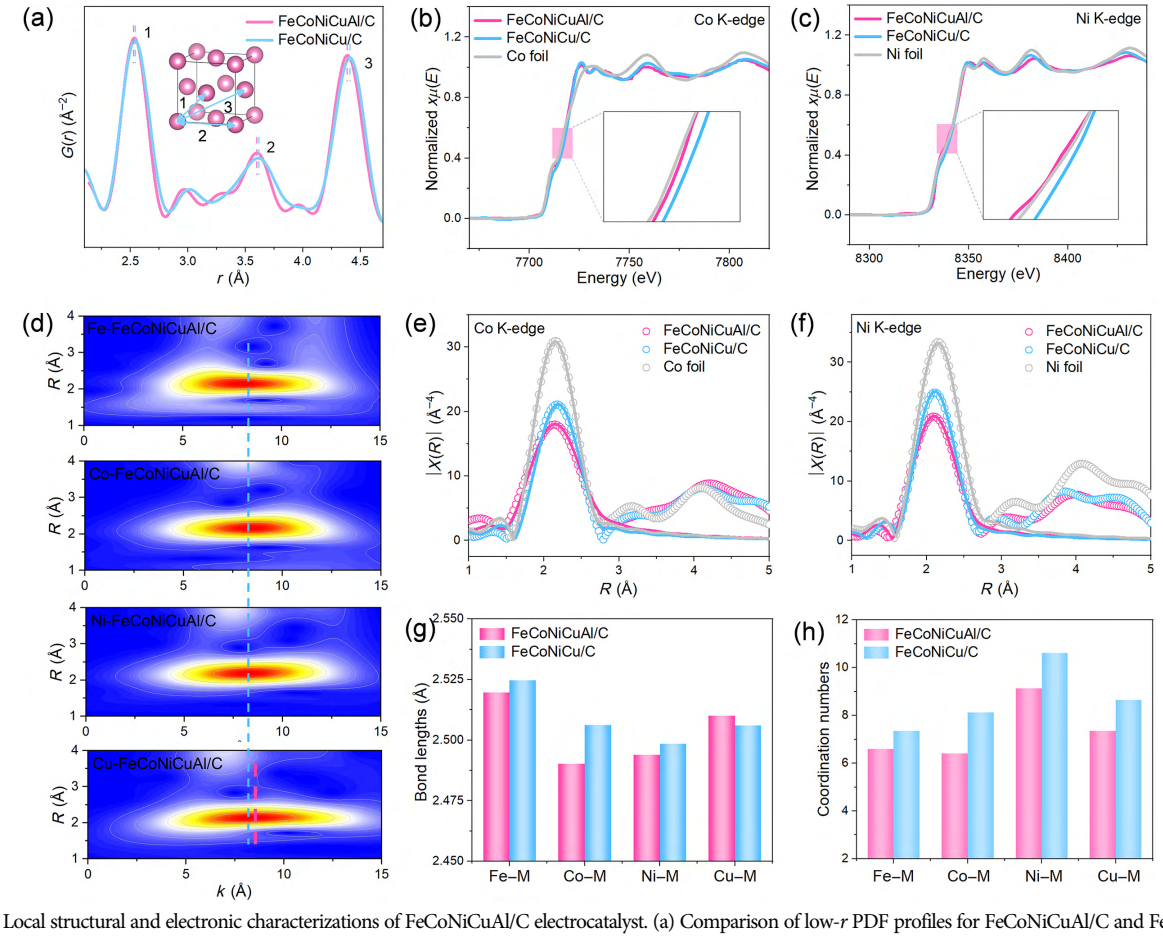

Figure 4 Local structural and electronic characterizations of FeCoNiCuAl/C electrocatalyst. (a) Comparison of low-r PDF profiles for FeCoNiCuAl/C and FeCoNiCu/C. (b) Normalized XANES spectra at Co and (c) Ni K-edges. (d) WT-EXAFS contour maps for Fe, Co, Ni, and Cu K-edges for FeCoNiCuAl/C. ((e) and (f)) k^3-weighted Fourier transform for EXAFS spectra of (e) Co and (f) Ni K-edges. ((g) and (h)) Comparison of (g) extracted first-shell bond lengths and (h) coordination numbers for Fe, Co, Ni, and Cu, comparing FeCoNiCuAl/C and FeCoNiCu/C.

We also performed *in situ* electrochemical Raman spectroscopy to investigate structural changes of FeCoNiCuAl/C during the OER process. As shown in Fig. S24 in the ESM, upon applying an anodic potential, new peaks emerge at ~ 294 and ~ 340 cm^{-1}, which can be ascribed to the formation of CuO [69, 70]. Notably, as the potential increases, only distinct Cu–O peaks are observed, with no detectable signals from other metal–oxygen species. The phenomenon is attributed to the oxidation of aggregated Cu, where the aggregation of Cu arises from the less negative Cu–Al mixing enthalpy and is consistent with the findings from the WT-EXAFS analysis. Due to the relatively higher surface energy of aggregated Cu, which renders Cu atoms more active, aggregated Cu is more prone to oxidation compared to the alloy [71, 72]. It is believed that the oxidation of aggregated Cu can improve electrochemical activity, as high-valence transition metals exhibit a strong hydrolysis effect to promote the formation of *OOH, which accelerates electrochemical kinetics [73].

To elucidate how Al incorporation enhances the intrinsic OER activity of FeCoNiCuAl/C, we performed DFT calculations on (111) slab models of FeCoNiCuAl and FeCoNiCu HEAs (Fig. S25 in the ESM, see computational details in Section 2). Projected density of states (PDOS, Fig. 5(a)) reveals that the overall d-band centers shift from −1.676 eV in FeCoNiCu to −1.615 eV in FeCoNiCuAl. This upshift brings the d-band closer to the Fermi level, reducing the occupation of antibonding states and thereby strengthening adsorbate binding, facilitating more efficient intermediate binding and subsequent reaction progression [74, 75], which is in consistent with the finding from EXAFS fittings analysis that reduced coordination numbers enhance adsorption capacity.

To identify the most favorable adsorption sites for H_2O molecule, the adsorption energies at all non-equivalent atop sites of individual metal atoms (including different surface atomic positions for each element) were systematically evaluated via DFT calculations. The screening results reveal that in FeCoNiCu, Fe exhibits the strongest adsorption (−0.98 eV), followed by Co (−0.87 eV), Ni (−0.62 eV), and Cu (−0.51 eV). In FeCoNiCuAl, Al demonstrats a higher adsorption energy (−0.64 eV) relative to the other metal elements (Tables S4 and S5 in the ESM). These quantitative results indicate the optimal adsorption sites are Fe in FeCoNiCu and Al in FeCoNiCuAl. Gibbs free energy (ΔG) diagrams for the four elementary OER steps were computed for both models. As shown in Figs. S26 and S27 in the ESM, although OH^- initially adsorbs at Al atop sites to form *OH, *OH can not stabilize at Al atop sites but instead prefer bridging sites between Al and neighboring M (Fe, Co, Ni, and Cu) atoms. Furthermore, as the OER reaction intermediate evolves from *OH to *O and then to *OOH, the adsorption sites on the catalyst surface correspondingly shift from the Al–M bridging site to the hollow site and back to the bridging site, accompanied by systematic changes in adsorption energy (Figs. 5(b) and 5(c)). These computational results provide direct evidence that the synergistic interaction between Al and neighboring metal sites facilitates the efficient OER. Notably, for both models, the highest energy barrier corresponds to *OOH desorption: ΔG (*OOH → O_2) is 5.12 eV on FeCoNiCu but is reduced to 2.00 eV on FeCoNiCuAl. This dramatic decrease confirms that Al-driven electronic modulation lowers the rate-limiting step, consistent with the PDOS analysis and the experimentally observed lower overpotentials and accelerated kinetics.

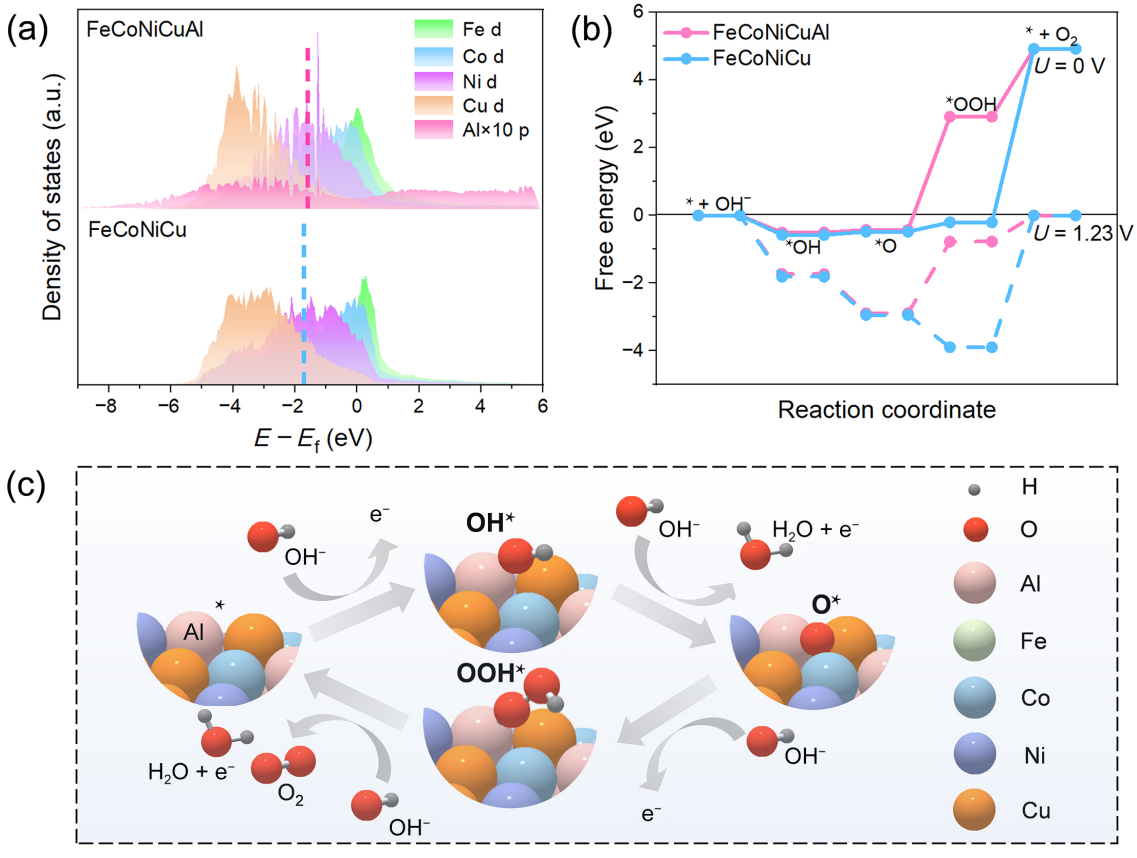

Figure 5 Density functional theory calculation for the OER mechanism. (a) PDOS and (b) Gibbs free energy diagrams of FeCoNiCuAl HEA electrocatalyst and FeCoNiCu. (c) Schematic of the whole OER mechanism on FeCoNiCuAl.

Overall, the superior OER performance of the FeCoNiCuAl/C nanoreactor arises from three synergistic factors. First, our ultrafast explosion-driven CTS method gives rise to a hierarchically porous carbon scaffold, containing continuous and interconnected nano-cavities that dramatically increase surface area and expose abundant active sites. Second, the simultaneous *in situ* nucleation and confinement of FeCoNiCuAl HEA NPs ensure uniform dispersion on both external and internal surfaces, maximizing catalyst utilization and facilitating rapid mass transport. Third, strategic incorporation of Al induces compressive strain and d-band modulation, which lowers the *OOH desorption barrier and enhances intrinsic activity. Together, these structural and electronic advantages endow FeCoNiCuAl/C with low overpotentials, accelerated kinetics, and long-term durability, establishing a versatile one-step route to high-entropy alloy nanoreactors for advanced water-splitting and energy-storage applications.

4 Conclusions

To summarize, we demonstrated a one-step ultrafast thermal explosion strategy to fabricate hierarchically porous carbon nanoreactors uniformly embedding FeCoNiCuAl HEA NPs. The resulting FeCoNiCuAl/C catalyst exhibits outstanding OER performance, including a low overpotential and great durability superior than commercial RuO_2. When applied to overall water splitting and Zn-air batteries, it achieves good performance, validating its practical applicability. Advanced HAADF-STEM and 3D tomography reconstruction reveal a continuous network of internal cavities and HEA NP confinement, while XAFS and DFT analyses show that the Al incorporation induces compressive strain, lowers coordination numbers, and modulates the d-band center to reduce the *OOH desorption barrier. Al and neighboring metal sites synergistically collaborate to complete the OER process. By integrating explosion-driven nanoreactor formation with HEA design, this work establishes a versatile strategy for noble-metal-free electrocatalysts design and paves the way for their deployment in efficient and durable energy-conversion technologies.

Electronic Supplementary Material: Supplementary material (FeCoNiCuAl HEA electrocatalyst structure characterization, overall water splitting and rechargeable Zn-air battery applications, *in situ* Raman spectra of the FeCoNiCuAl/C at different potentials, and the surface models of DFT calculations) is available in the online version of this article at https://doi.org/10.26599/NR.2026.94908613.

Data availability

All data needed to support the conclusions in the paper are presented in the manuscript and the Electronic Supplementary Material. Additional data related to this paper may be requested from the corresponding author upon request.

Acknowledgements

This study was financially supported by the National Natural Science Foundation of China (Nos. 22275089, 52222104, 12261160364, and 52573263), the Basic Research Program of Jiangsu (No. BK20253026), and the Fundamental Research Funds for the Central Universities (Nos. 30922010307 and 30925020216). We thank the BL13SSW beamline at the Shanghai Synchrotron Radiation Facility (https://cstr.cn/31124.02.SSRF. BL13SSW) for the XAFS and PDF experiments supports.

Declaration of competing interest

All the contributing authors report no conflict of interests in this work.

Author contribution statement

X. D. Z.: Conceptualization, data curation, formal analysis, project administration, writing – original draft, writing – review & editing. F. X.: Formal analysis, validation, writing – original draft. H. Z.: Funding acquisition, resources, supervision, writing – review & editing. W. H.: Conceptualization, formal analysis. H. R. Y.: Conceptualization, formal analysis. S. M. P.: Data curation. W.-D. L.: Resources, supervision, writing – review & editing. R. H. Y.: Formal analysis, methodology. J. R. Z.: Formal analysis, methodology. S. L.: Funding acquisition, resources, supervision, writing – review & editing. All the authors have approved the final manuscript.

Use of AI statement

None.

References

[1] Oener, S. Z.; Bergmann, A.; Cuenya, B. R. Designing active oxides for a durable oxygen evolution reaction. *Nat. Synth.* **2023**, *2*, 817–827.

[2] Zhou, X. C.; Chen, S. Q.; Zhou, M. J.; Li, M.; Lan, S.; Feng, T. Highly efficient cobalt-based amorphous catalyst for peroxymonosulfate activation toward wastewater remediation. *Rare Met.* **2023**, *42*, 1160–1174.

[3] Terlouw, T.; Bauer, C.; McKenna, R.; Mazzotti, M. Large-scale hydrogen production via water electrolysis: A techno-economic and environmental assessment. *Energy Environ. Sci.* **2022**, *15*, 3583–3602.

[4] Nguyen, T. X.; Su, Y. H.; Lin, C. C.; Ruan, J.; Ting. J. M. A new high entropy glycerate for high performance oxygen evolution reaction. *Adv. Sci.* **2021**, *8*, 2002446.

[5] Wang, X. P.; Zhong, H. Y.; Xi, S. B.; Lee, W. S. V.; Xue, J. M. Understanding of oxygen redox in the oxygen evolution reaction. *Adv. Mater.* **2022**, *34*, 2107956.

[6] Sharma, L.; Katiyar, N. K.; Parui, A.; Das, R.; Kumar, R.; Tiwary, C. S.; Singh, A. K.; Halder, A.; Biswas, K. Low-cost high entropy alloy (HEA) for high-efficiency oxygen evolution reaction (OER). *Nano Res.* **2022**, *15*, 4799–4806.

[7] Retuerto, M.; Pascual, L.; Torrero, J.; Salam, M. A.; Tolosana-Moranchel, Á.; Gianolio, D.; Ferrer, P.; Kayser, P.; Wilke, V.; Stiber, S. et al. Highly active and stable OER electrocatalysts derived from Sr_2MIrO_6 for proton exchange membrane water electrolyzers. *Nat. Commun.* **2022**, *13*, 7935.

[8] Deka, N.; Jones, T. E.; Falling, L. J.; Sandoval-Diaz, L. E.; Lunkenbein, T.; Velasco-Velez, J. J.; Chan, T. S.; Chuang, C. H.; Knop-Gericke, A.; Mom, R. V. On the operando structure of ruthenium oxides during the oxygen evolution reaction in acidic media. *ACS Catal.* **2023**, *13*, 7488–7498.

[9] Oh, N. K.; Seo, J.; Lee, S.; Kim, H. J.; Kim, U.; Lee, J.; Han, Y. K.; Park, H. Highly efficient and robust noble-metal free bifunctional water electrolysis catalyst achieved via complementary charge transfer. *Nat. Commun.* **2021**, *12*, 4606.

[10] He, R. L.; He, J. K.; Pu, K.; Li, Q. L.; Liu, F.; Chen, Q. W.; Liu, W. Q.; Chen, H.; Chai, H.; Bao, S. J. et al. Boosting OER activity of Fe-N

moieties via Ni induced d-orbital tailoring for durable rechargeable Zn-air batteries. *Chem. Eng. J.* **2024**, *500*, 156754.
[11] Dai, W. J.; Lu, T.; Pan, Y. Novel and promising electrocatalyst for oxygen evolution reaction based on MnFeCoNi high entropy alloy. *J. Power Sources* **2019**, *430*, 104–111.
[12] Zhang, Z. J.; Guo, J. P.; Sun, S. H.; Sun, Q.; Zhao, Y. W.; Zhang, Y. F.; Yu, Z. Y.; Li, C. S.; Sun, Y.; Zhang, M. M. et al. Optimized valence state of Co and Ni in high-entropy alloy for high active-stable OER. *Rare Met.* **2023**, *42*, 3607–3613.
[13] Zhang, W. T.; Wang, X. Q.; Zhang, F. Q.; Cui, X. Y.; Fan, B. B.; Guo, J. M.; Guo, Z. M.; Huang, R.; Huang, W.; Li, X. B. et al. Frontiers in high entropy alloys and high entropy functional materials. *Rare Met.* **2024**, *43*, 4639–4776.
[14] Nandan, R.; Rekha, M. Y.; Devi, H. R.; Srivastava, C.; Nanda, K. K. High-entropy alloys for water oxidation: A new class of electrocatalysts to look out for. *Chem. Commun.* **2021**, *57*, 611–614.
[15] Hao, J. C.; Zhuang, Z. C.; Cao, K. C.; Gao, G. H.; Wang, C.; Lai, F. L.; Lu, S. L.; Ma, P. M.; Dong, W. F.; Liu, T. X. et al. Unraveling the electronegativity-dominated intermediate adsorption on high-entropy alloy electrocatalysts. *Nat. Commun.* **2022**, *13*, 2662.
[16] Luo, M. C.; Guo, S. J. Strain-controlled electrocatalysis on multimetallic nanomaterials. *Nat. Rev. Mater.* **2017**, *2*, 17059.
[17] Dong, C. Y.; Gao, Z. R.; Li, Y. L.; Peng, M.; Wang, M.; Xu, Y.; Li, C. Y.; Xu, M.; Deng, Y. C.; Qin, X. T. et al. Fully exposed palladium cluster catalysts enable hydrogen production from nitrogen heterocycles. *Nat. Catal.* **2022**, *5*, 485–493.
[18] Huang, K.; Peng, D. D.; Yao, Z. X.; Xia, J. Y.; Zhang, B. W.; Liu, H.; Chen, Z. B.; Wu, F.; Wu, J.; Huang, Y. S. et al. Cathodic plasma driven self-assembly of HEAs dendrites by pure single FCC FeCoNiMnCu nanoparticles as high efficient electrocatalysts for OER. *Chem. Eng. J.* **2021**, *425*, 131533.
[19] He, R.; Yang, L. L.; Zhang, Y.; Wang, X.; Lee, S.; Zhang, T.; Li, L. X.; Liang, Z. F.; Chen, J. W.; Li, J. S. et al. A CrMnFeCoNi high entropy alloy boosting oxygen evolution/reduction reactions and zinc-air battery performance. *Energy Storage Mater.* **2023**, *58*, 287–298.
[20] Kwon, J.; Sun, S.; Choi, S.; Lee, K.; Jo, S.; Park, K.; Kim, Y. K.; Park, H. B.; Park, H. Y.; Jang, J. H. et al. Tailored electronic structure of Ir in high entropy alloy for highly active and durable bifunctional electrocatalyst for water splitting under an acidic environment. *Adv. Mater.* **2023**, *35*, 2300091.
[21] Li, M. G.; Lin, F. X.; Zhang, S. P.; Zhao, R.; Tao, L.; Li, L.; Li, J. Y.; Zeng, L. Y.; Luo, M. C.; Guo, S. J. High-entropy alloy electrocatalysts go to (sub-)nanoscale. *Sci. Adv.* **2024**, *10*, eadn2877.
[22] Yan, X. Y.; Zhou, Y. S.; Wang, S. Y. Nano-high entropy materials in electrocatalysis. *Adv. Funct. Mater.* **2025**, *35*, 2413115.
[23] Ravi, R.; Bakshi, S. R. Microstructural evolution and wear behavior of carbon added CoCrFeMnNi multi-component alloy fabricated by mechanical alloying and spark plasma sintering. *J. Alloys Compd.* **2021**, *883*, 160879.
[24] Jia, Z.; Nomoto, K.; Wang, Q.; Kong, C.; Sun, L. G.; Zhang, L. C.; Liang, S. X.; Lu, J.; Kruzic, J. J. A self-supported high-entropy metallic glass with a nanosponge architecture for efficient hydrogen evolution under alkaline and acidic conditions. *Adv. Funct. Mater.* **2021**, *31*, 2101586.
[25] Han, C. X.; Zhi, J. Q.; Zeng, Z.; Wang, Y. S.; Zhou, B.; Gao, J.; Wu, Y. X.; He, Z. Y.; Wang, X. M.; Yu, S. W. Synthesis and characterization of nano-polycrystal diamonds on refractory high entropy alloys by chemical vapour deposition. *Appl. Surf. Sci.* **2023**, *623*, 157108.
[26] Zhu, G. H.; Jiang, Y.; Yang, H. Y.; Wang, H. F.; Fang, Y.; Wang, L.; Xie, M.; Qiu, P. P.; Luo, W. Constructing structurally ordered high-entropy alloy nanoparticles on nitrogen-rich mesoporous carbon nanosheets for high-performance oxygen reduction. *Adv. Mater.* **2022**, *34*, 2110128.
[27] Zhu, X. D.; Huang, W.; Lou, Y.; Yao, Z. Z.; Ying, H. Q.; Dong, M.; Tan, L.; Zeng, J. R.; Ji, H.; Zhu, H. et al. Ultrafast joule-heating synthesis of FeCoMnCuAl high-entropy-alloy nanoparticles as efficient OER electrocatalysts. *Prog. Nat. Sci.* **2024**, *34*, 880–887.
[28] Yao, Y. G.; Huang, Z. N.; Xie, P. F.; Lacey, S. D.; Jacob, R. J.; Xie, H.; Chen, F. J.; Nie, A. M.; Pu, T. C.; Rehwoldt, M. et al. Carbothermal shock synthesis of high-entropy-alloy nanoparticles. *Science* **2018**, *359*, 1489–1494.
[29] Huang, W.; Zhu, X. D.; Zhu, H.; Wang, Z. H.; Yu, H. R.; Shao, Y.; Liu, Q.; Lan, S. High temperature shock (HTS) synthesis of carbon-based nanomaterials for electrochemical applications. *Carbon Neutralization* **2025**, *4*, e189.
[30] Cha, J. H.; Cho, S. H.; Kim, D. H.; Jeon, D.; Park, S.; Jung, J. W.; Kim, I. D.; Choi, S. Y. Flash-thermal shock synthesis of high-entropy alloys toward high-performance water splitting. *Adv. Mater.* **2023**, *35*, 2305222.
[31] Zhu, X. D.; Huang, W.; Tan, L.; Yao, Z. Z.; Yang, X.; Song, R. Y.; Chen, M. X.; Liu, D.; Zeng, J. R.; Zhu, H. et al. Ultrafast synthesis of tetragonal-distorted FeCoNiCuCr high-entropy alloy nanoparticles for enhanced OER performance. *Chin. Chem. Lett.* **2026**, *37*, 110852.
[32] Prescher, C.; Prakapenka, V. B. *DIOPTAS*: A program for reduction of two-dimensional X-ray diffraction data and data exploration. *High Press. Res.* **2015**, *35*, 223–230.
[33] Qiu, X.; Thompson, J. W.; Billinge, S. J. L. *PDFgetX2*: A GUI-driven program to obtain the pair distribution function from X-ray powder diffraction data. *J. Appl. Cryst.* **2004**, *37*, 678.
[34] Farrow, C. L.; Juhas, P.; Liu, J. W.; Bryndin, D.; Božin, E. S.; Bloch, J.; Proffen, T.; Billinge, S. J. L. PDFfit2 and PDFgui: Computer programs for studying nanostructure in crystals. *J. Phys. Condens. Matter* **2007**, *19*, 335219.
[35] Ravel, B.; Newville, M. ATHENA, ARTEMIS, HEPHAESTUS: Data analysis for X-ray absorption spectroscopy using IFEFFIT. *J. Synchrotron Radiat.* **2005**, *12*, 537–541.
[36] Funke, H.; Scheinost, A. C.; Chukalina, M. Wavelet analysis of extended X-ray absorption fine structure data. *Phys. Lett. B* **2005**, *71*, 094110.
[37] Sun, X. G.; Shen, W.; Liu, H.; Xi, P. X.; Jaroniec, M.; Zheng, Y.; Qiao, S. Z. Corrosion-resistant NiFe anode towards kilowatt-scale alkaline seawater electrolysis. *Nat. Commun.* **2024**, *15*, 10351.
[38] Kaur, S. P.; Mishra, V.; Chakraborty, B. Transition metal dichalcogenides and hybrids for electrochemical sensing. In *2D Materials-Based Electrochemical Sensors*. Rout, C. S., Ed.; Elsevier: Amsterdam, 2023, pp 199–224.
[39] van de Walle, A.; Tiwary, P.; de Jong, M.; Olmsted, D. L.; Asta, M.; Dick, A.; Shin, D.; Wang, Y.; Chen, L. Q.; Liu, Z. K. Efficient stochastic generation of special quasirandom structures. *Calphad* **2013**, *42*, 13–18.
[40] Xue, F.; Li, Q.; Ji, W. H.; Lv, M. X.; Xu, H. K.; Zeng, J. R.; Li, T. Y.; Ren, Y.; Zhou, L. H.; Chen, X. et al. Highly efficient semi-hydrogenation in strained ultrathin PdCu shell and the atomic deciphering for the unlocking of activity–selectivity. *Chem. Sci.* **2024**, *15*, 11837–11846.
[41] Wang, X. Y. ; Liu, Q. D.; Wang, X. High-entropy materials: From bulk to sub-nano. *Adv. Funct. Mater.* **2025**, *35*, 2504275.
[42] Shi, W. H.; Liu, H. W.; Zhang, J. W.; Shen, S. Y.; Wang, Y. H.; Guo, Y. Q.; Yue, K. H.; Liang, Z. H.; Zhang, H.; Zhang, L. et al. Roll-to-roll synthesis of multielement heterostructured catalysts. *Nat. Synth.* **2025**, *4*, 836–847.
[43] Wang, H.; He, Q. F.; Gao, X.; Shang, Y. H.; Zhu, W. Q.; Zhao, W. J.; Chen, Z. Q.; Gong, H.; Yang, Y. Multifunctional high entropy alloys enabled by severe lattice distortion. *Adv. Mater.* **2024**, *36*, 2305453.
[44] Moradi, M.; Hasanvandian, F.; Bahadoran, A.; Shokri, A.; Zerangnasrabad, S.; Kakavandi, B. New high-entropy transition-metal sulfide nanoparticles for electrochemical oxygen evolution reaction. *Electrochim. Acta* **2022**, *436*, 141444.
[45] Wei, H. H.; Wang, Q.; Zhang, Y.; Li, J.; Liu, P.; Wang, N. N.; Gong, X. Q. Engineering high-entropy alloy nanosheets toward efficient electrocatalytic water oxidation. *Fuel* **2024**, *358*, 130011.
[46] Liu, G. Y.; Yao, R. Y.; You, J. H.; Liu, L. L.; Yi, B. L.; Zhao, Y.; Li,

Y. H.; Zhang, H. Z. Non-precious metal high-entropy electrocatalysts ($Al_{0.5}$NiCoCr-$X_{0.5}$) for OER application. *Mater. Today Commun.* **2024**, *39*, 109052.

[47] Zhang, Y.; Dai, W. J.; Zhang, P. F.; Lu, T.; Pan, Y. *In-situ* electrochemical tuning of $(CoNiMnZnFe)_3O_{3.2}$ high-entropy oxide for efficient oxygen evolution reactions. *J. Alloys Compd.* **2021**, *868*, 159064.

[48] Pathan, S. C.; Shaikh, J. S.; Rittiruam, M.; Saelee, T.; Márquez, V.; Khajondetchairit, P.; Mali, S. S.; Patil, J. V.; Hong, C. K.; Praserthdam, P. et al. High entropy metal oxide/TiO_2 nanocomposite for electrocatalytic overall water splitting. *J. Alloys Compd.* **2024**, *1008*, 176811.

[49] Alamdari, A. A.; Jahangiri, H.; Yagci, M. B.; Igarashi, K.; Matsumoto, H.; Motallebzadeh, A.; Unal, U. Exploring the role of Mo and Mn in improving the OER and HER performance of CoCuFeNi-based high-entropy alloys. *ACS Appl. Energy Mater.* **2024**, *7*, 2423–2435.

[50] Liu, L. H.; Li, N.; Han, M.; Han, J. R.; Liang, H. Y. Scalable synthesis of nanoporous high entropy alloys for electrocatalytic oxygen evolution. *Rare Met.* **2022**, *41*, 125–131.

[51] Huang, K.; Zhang, B. W.; Wu, J. S.; Zhang, T. Y.; Peng, D. D.; Cao, X.; Zhang, Z.; Li, Z.; Huang, Y. Z. Exploring the impact of atomic lattice deformation on oxygen evolution reactions based on a sub-5 nm pure face-centred cubic high-entropy alloy electrocatalyst. *J. Mater. Chem. A* **2020**, *8*, 11938–11947.

[52] Chen, Z. B.; Huang, K.; Zhang, B. W.; Xia, J. Y.; Wu, J. S.; Zhang, Z. Q.; Huang, Y. Z. Corrosion engineering on AlCoCrFeNi high-entropy alloys toward highly efficient electrocatalysts for the oxygen evolution of alkaline seawater. *Int. J. Miner. Metall. Mater.* **2023**, *30*, 1922–1932.

[53] Huang, J. B.; Jiang, Y.; An, T. Y.; Cao, M. H. Increasing the active sites and intrinsic activity of transition metal chalcogenide electrocatalysts for enhanced water splitting. *J. Mater. Chem. A* **2020**, *8*, 25465–25498.

[54] Huang, H. W.; Cho, A.; Kim, S.; Jun, H.; Lee, A.; Han, J. W.; Lee, J. Structural design of amorphous $CoMoP_x$ with abundant active sites and synergistic catalysis effect for effective water splitting. *Adv. Funct. Mater.* **2020**, *30*, 2003889.

[55] Chen, L. L.; Li, M. H.; Zhang, J. N. Tailoring microenvironment for efficient CO_2 electroreduction through nanoconfinement strategy. *Nano Res.* **2024**, *17*, 7880–7899.

[56] Kim, O. H.; Cho, Y. H.; Kang, S. H.; Park, H. Y.; Kim, M.; Lim, J. W.; Chung, D. Y.; Lee, M. J.; Choe, H.; Sung, Y. E. Ordered macroporous platinum electrode and enhanced mass transfer in fuel cells using inverse opal structure. *Nat. Commun.* **2013**, *4*, 2473.

[57] Ma, Y. Z.; Li, H. T.; Liu, J.; Zhao, D. Y. Understanding the chemistry of mesostructured porous nanoreactors. *Nat. Rev. Chem.* **2024**, *8*, 915–931.

[58] Wan, X.; Liu, X. F.; Li, Y. C.; Yu, R. H.; Zheng, L. R.; Yan, W. S.; Wang, H.; Xu, M.; Shui, J. L. Fe-N-C electrocatalyst with dense active sites and efficient mass transport for high-performance proton exchange membrane fuel cells. *Nat. Catal.* **2019**, *2*, 259–268.

[59] Du, H. G.; Zhang, X. F.; Ding, L. W.; Liu, J. L.; Yu, L. H.; Zhang, X. H.; Dou, Y. H.; Cao, L. M.; Zhang, J.; He, C. T. Engineering pore-size distribution of metal-loaded carbon catalysts by *in situ* cavitation for boosting electrochemical mass transfer. *Appl. Catal. B Environ.* **2024**, *342*, 123396.

[60] Yu, Z. H.; Ji, N.; Li, X. Y.; Zhang, R.; Qiao, Y. N.; Xiong, J.; Liu, J.; Lu, X. B. Kinetics driven by hollow nanoreactors: An opportunity for controllable catalysis. *Angew. Chem., Int. Ed.* **2023**, *62*, e202213612.

[61] Rong, C. L.; Dastafkan, K.; Wang, Y.; Zhao, C. Breaking the activity and stability bottlenecks of electrocatalysts for oxygen evolution reactions in acids. *Adv. Mater.* **2023**, *35*, 2211884.

[62] Zhu, W.; Chen, Z.; Pan, Y.; Dai, R. Y.; Wu, Y.; Zhuang, Z. B.; Wang, D. S.; Peng, Q.; Chen, C.; Li, Y. D. Functionalization of hollow nanomaterials for catalytic applications: Nanoreactor construction. *Adv. Mater.* **2019**, *31*, 1800426.

[63] Jiao, S. L.; Fu, X. W.; Huang, H. W. Descriptors for the evaluation of electrocatalytic reactions: D-Band theory and beyond. *Adv. Funct. Mater.* **2022**, *32*, 2107651.

[64] Li, D. Y.; Zhao, L. L.; Wang, J.; Yang, C. P. Tailoring the d-band center over isomorphism pyrite catalyst for optimized intrinsic affinity to intermediates in lithium-oxygen batteries. *Adv. Energy Mater.* **2023**, *13*, 2204057.

[65] Takeuchi, A.; Inoue, A. Classification of bulk metallic glasses by atomic size difference, heat of mixing and period of constituent elements and its application to characterization of the main alloying element. *Mater. Trans.* **2005**, *46*, 2817–2829.

[66] Bai, J. R.; Sun, Z. Z.; Zhang, H. Y.; Lian, Y. B.; Deng, Y. Y.; Xiang, M.; Su, Y. Q. Modulating the local coordination environment of M-N_x single-atom site for enhanced electrocatalytic oxygen reduction. *Adv. Funct. Mater.* **2025**, *35*, 2417013.

[67] Tomboc, G. M.; Kim, T.; Jung, S.; Yoon, H. J.; Lee, K. Modulating the local coordination environment of single-atom catalysts for enhanced catalytic performance in hydrogen/oxygen evolution reaction. *Small* **2022**, *18*, 2105680.

[68] Khorshidi, A.; Violet, J.; Hashemi, J.; Peterson, A. A. How strain can break the scaling relations of catalysis. *Nat. Catal.* **2018**, *1*, 263–268.

[69] Fan, Z. Y.; Yang, Q. Q.; Zhang, W. J.; Wen, H. M.; Meng, K. W.; Zhao, E.; Dong, L.; Yuan, H. Y.; Yang, H. G.; Chen, Z. P. Unravelling the dynamic modulation of copper (oxy)hydroxides for electrocatalytic organic nucleophile oxidation. *Angew. Chem., Int. Ed.* **2025**, *64*, e202516322.

[70] Ren, X. X.; Wang, J. J.; Wu, H.; Zhang, J. F.; Mao, J.; Wang, Z. Y.; Sun, K. H.; Chen, Y.; Zheng, X. R.; Han, X. P. et al. Cu–O geometric coordination induced facet evolution of derived Cu catalysts for efficient CO_2 electroreduction. *Sci. China Mater.* **2025**, *68*, 3322–3331.

[71] Gao, L. K.; Cui, X.; Sewell, C. D.; Li, J.; Lin, Z. Q. Recent advances in activating surface reconstruction for the high-efficiency oxygen evolution reaction. *Chem. Soc. Rev.* **2021**, *50*, 8428–8469.

[72] Men, Y. A.; Wu, D. A.; Hu, Y. C.; Li, L.; Li, P.; Jia, S. F.; Wang, J. B.; Cheng, G. Z.; Chen, S. L.; Luo, W. Understanding alkaline hydrogen oxidation reaction on PdNiRuIrRh high-entropy-alloy by machine learning potential. *Angew. Chem., Int. Ed.* **2023**, *62*, e202217976.

[73] Li, L.; Cao, X. J.; Huo, J. J.; Qu, J. P.; Chen, W. H.; Liu, C. T.; Zhao, Y. F.; Liu, H.; Wang, G. X. High valence metals engineering strategies of Fe/Co/Ni-based catalysts for boosted OER electrocatalysis. *J. Energy Chem.* **2023**, *76*, 195–231.

[74] Chen, J. H.; Ma, J. L.; Huang, T.; Liu, Q. C.; Liu, X. K.; Luo, R. H.; Xu, J. W.; Wang, X. Y.; Jiang, T. L.; Liu, H. X. et al. Iridium-free high-entropy alloy for acidic water oxidation at high current densities. *Angew. Chem., Int. Ed.* **2025**, *64*, e202503330.

[75] Wang, S. Q.; Xu, B. L.; Huo, W. Y.; Feng, H. C.; Zhou, X. F.; Fang, F.; Xie, Z. H.; Shang, J. K.; Jiang, J. Q. Efficient FeCoNiCuPd thin-film electrocatalyst for alkaline oxygen and hydrogen evolution reactions. *Appl. Catal. B Environ.* **2022**, *313*, 121472.